Geophys. J. Int. (0000) **000**, 000–000

Shear Wave Structure of a Transect of the Los Angeles Basin From Multimode Surface Waves and H/V Spectral Ratio Analysis

Mathieu Perton[1], Zack J. Spica[2], Robert W. Clayton[3] and Gregory C. Beroza[4]
[1] *Instituto de Ingeniería, Universidad Nacional Autónoma de México, Circuito Escolar s/n, Cd Universitaria, Coyoacán 04510, CDMX, Mexico*
[2] *Department of Earth and Environmental Sciences, University of Michigan, Ann Arbor, MI 48109, USA.*
[3] *Seismological Laboratory, California Institute of Technology, Pasadena, California 91125, USA.*
[4] *Department of Geophysics, 397 Panama Mall, Stanford University, Stanford, California 94305-2215, USA.*
Mathieu Pertonmathieu.perton@gmail.com

9 October 2019

SUMMARY
We use broadband stations of the 'Los Angeles Syncline Seismic Interferometry Experiment' (LASSIE) to perform a joint inversion of the Horizontal to Vertical spectral ratios (H/V) and multimode dispersion curves (phase and group velocity) for both Rayleigh and Love waves at each station of a dense line of sensors. The H/V of the auto-correlated signal at a seismic station is proportional to the ratio of the imaginary parts of the Green's function. The presence of low-frequency peaks (∼0.2 Hz) in H/V allows us to constrain the structure of the basin with high confidence to a depth of 6 km. The velocity models we obtain are broadly consistent with the SCEC CVM-H community model and agree well with known geological features. Because our approach differs substantially from previous modeling of crustal velocities in southern California, this research validates both the utility of the diffuse field H/V measurements for deep structural characterization and the predictive value of the CVM-H community velocity model in the Los Angeles region. We also analyze a lower frequency peak (∼0.03 Hz) in H/V and suggest it could be the signature of the Moho. Finally, we show that the independent comparison of the H and V components with their corresponding theoretical counterparts gives information about the degree of diffusivity of the ambient seismic field.

Key words: Tomography; Seismic noise; Site effect; HVSR; surface waves.

1 INTRODUCTION

Much of metropolitan Los Angeles (Fig 1) is situated atop sedimentary basins. The Los Angeles Basin (LA Basin) is the largest of these and understanding its seismic response is of fundamental importance for mitigating the risk caused to one of the most populated regions in the US. Sedimentary basins are known to influence dramatically the distribution of damage from earthquake shaking by increasing the amplitude and duration of ground motion, and by responding nonlinearly to incident seismic waves (e.g. Cruz-Atienza et al. 2016). Multiple ground motion simulation efforts (Olsen 2000; Olsen et al. 2006, 2009; Komatitsch et al. 2004; Graves et al. 2011), along with independent ambient-field measurements (Denolle et al. 2014) have confirmed such behavior for the Los Angeles Basin, especially in the 2-5 s period range, which poses a substantial risk to tall buildings and other long-period structures. The predictive value of simulations depends critically on the accuracy of structural representations of these basins (e.g. Wald & Graves 1998), which motivates continuing efforts to constrain their structure.
Significant progress has been made toward the goal of developing a unified velocity structure for Southern California. Special emphasis on the Los Angeles region started initially with data from the energy industry, which continues to provide data (e.g. Lin et al. 2013; Nakata et al. 2015). Magistrale et al. (2000) used a combination of receiver functions (Zhu & Kanamori 2000), geotechnical data (Magistrale et al. 1996) and tomography (Hauksson 2000) to produce the first Community Velocity Model, known as CVM-S. To determine the shape of the sedimentary section of the LA Basin, Süss & Shaw (2003) used *P*-wave

[!th]

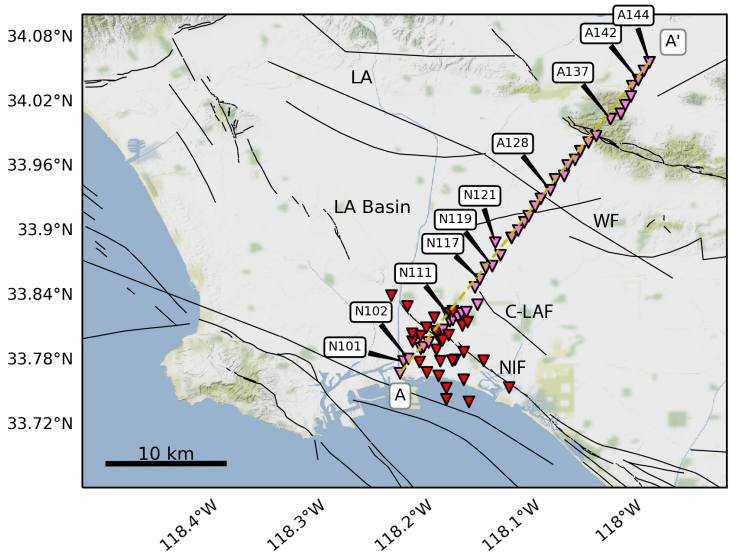

Figure 1. The LASSIE array and the Los Angeles basin area. The red and pink triangles are the broad-band stations of the LASSIE 1 and LASSIE 2 arrays, respectively. Only the structure below the 43 stations of the linear array is assessed. The yellow dashed line denotes the location of the profile A–A'. The faults are shown in black lines (from Jennings & Bryant 2010). Seismic stations for which we provide deeper analysis are highlighted with their names. LA: Los Angeles; LA Basin: Los Angeles Basin; WF: Whittier Fault; C-LAF: Compton-Los Alamitos Fault; NIF: Newport-Inglewood Fault.

velocity measurements derived from stacking velocities obtained from reflection surveys and calibrated them with numerous borehole sonic logs. These models were spliced together and further refined through full-waveform inversion (Tape et al. 2009; Lee et al. 2014), leading to a unified model (Shaw et al. 2015) : the SCEC Community Velocity Model - Harvard (CVM-H, version 15.1.0).

Because the ambient seismic field (ASF) can be measured wherever seismic stations are located, and at whatever density they are deployed, it plays an increasingly important role in constraining crustal structure (Shapiro et al. 2005; Lin et al. 2013; Bowden et al. 2015; Nakata et al. 2015; Ma & Clayton 2016; Berg et al. 2018). With dense arrays, both high-frequency surface waves (e.g. Lin et al. 2013; Spica et al. 2018b) and body waves (Nakata et al. 2015; Spica et al. 2018b) can be extracted and used to determine the velocity of the shallow crust. The high-frequency surface waves extracted from ASF are often composed of both fundamental and higher modes (e.g. Savage et al. 2013; Rivet et al. 2015; Ma et al. 2016; Spica et al. 2018b,a; Tomar et al. 2018), which means they are rich in information, but also that potential points of osculation (touching) in the dispersion curves (DC) can lead to incorrect mode branch identification (Spica et al. 2018a). Ma et al. (2016) used the 'Los Angeles Syncline Seismic Interferometry Experiment' array (LASSIE; Fig. 1; LASSIE (2014)) to show that higher modes are a strong component of high-frequency Rayleigh waves. They proposed that the separation of different mode branches can be accomplished through a particle motion filter. In a companion paper Ma & Clayton (2016) used the fundamental mode of both Love and Rayleigh waves along with receiver-function analysis to provide new constraints on the 2-D V_S structure of the LA Basin. They noted that the shallow structure (less than 10 km depth) presents strong lateral variations near fault lines, which should have a significant impact on the seismic wavefield.

In addition to the use of long-range correlation between pairs of stations, Sánchez-Sesma et al. (2011) showed that a single three-component short-time measurements of ASF can be used to assess the geological structure through the Horizontal-to-Vertical spectral ratio (HVSR or H/V) (e.g. Spica et al. 2015; García-Jerez et al. 2016; Piña-Flores et al. 2016; Perton et al. 2017). While H/V is traditionally considered to be only sensitive to the shallow-surface (i.e. the first 200 m) (Nakamura 1989) or to intermediate depth (Asten et al. 2014) , recent studies demonstrated the feasibility of modeling it to image deep interfaces down to several kilometers (Spica et al. 2015, 2018a). One well-known problem is that H/V measurement at the surface is generally insufficient to characterize shallow properties because a proportional change in layer velocities and thicknesses leads to similar H/V (e.g. Piña-Flores et al. 2016). Independent information, such as surface wave dispersion (Scherbaum et al. 2003; Piña-Flores et al. 2016; Lontsi et al. 2016) or H/V measurements recorded at different depths (Lontsi et al. 2015; Spica et al. 2017b) or locations (Perton et al. 2017) all provide opportunities to reduce this non-uniqueness. Additionally, Perton et al. (2017) suggested that the H and V components could be considered independently to assess the reliability of H/V and

to characterize properties of the noise field illumination.

Surface wave DC extracted from the ASF are sensitive to the absolute velocity and different modes provide different depth sensitivity, which provides further constraints on the velocity model (Tomar et al. 2018; Spica et al. 2018a); however, dispersion analysis may suffer from uncertainty due to mode misidentification and also tends to smooth the model properties along depth. H/V is primarily sensitive to sharp shear wave velocity contrasts and vertical travel-times, and thus offers a complimentary measurement.

We use data from the relatively dense LASSIE array composed of 71 broad-band sensors that traversed the Los Angeles Basin (LASSIE 2014). Fig. 1 shows the location of the temporary deployment of 43 stations in a line with ∼1 km inter-station distance (i.e., LASSIE 2). Stations recorded continuous seismic wavefield for about 40 days starting in September 2014. We use these data to determine a 2-D V_S profile of the Los Angeles Basin down to 6 km depth by means of a novel joint inversion procedure that involves H/V, multi-mode Love- and Rayleigh-wave dispersion at each station of the linear array. Finally, we show that H/V frequency peaks under 0.1 Hz are sensitive to the Moho discontinuity.

2 DATA PROCESSING

A traditional approach to infer the V_S structure under a station of a linear array using ASF would be to pursue surface wave tomography at different periods and then estimate a localized 1-D DC obtained at the closest grid point to the station (e.g. Ma & Clayton 2016). This approach can be applied for both Rayleigh and Love waves. As discussed in Ma & Clayton (2016), the energy in the Rayleigh waves in the Los Angeles Basin may spread over several overtones, while the modal content of the Loves waves is simpler. The application of Rayleigh wave tomography requires careful mode identification in the frequency-time diagrams. Ma & Clayton (2016) proposed using the retrograde ellipticity of the Rayleigh wave as a time-domain filter to isolate the fundamental modes of the GF and use them for tomography; however, when the velocity structure has a strong velocity-density gradient, the Rayleigh fundamental mode can switch to prograde ellipticity (Tanimoto & Rivera 2005; Denolle et al. 2012), making the time-domain filter approach ambiguous. Additional complication occurs at osculation points, where energy leaks between mode branches and where the time-domain filter becomes inefficient.

We propose an alternative blind, multi-mode identification in the frequency-velocity diagrams computed from local correlation functions computed by Ma & Clayton (2016). As described in Spica et al. (2018a), this approach avoids mode selection and better samples local heterogeneities than regionalized 1-D DC from tomographic inversion, which tends to smooth heterogeneities.

At a given station S, we select all the correlation functions from station-pairs located inside an area of 15 km radius centered on S. We use all the stations from the LASSIE 1 and 2 experiments in Fig. 1. For each station pair of inter-station length L, the center of the segment L must be distant from S by at most $D < L/6$ (except at both ends of the linear array where the selection criterion is lowered to $L/2$) to ensure that S is close to the center of the segment and primarily sensitive to local heterogeneity (Fig. 2C). We apply a frequency-time analysis (FTAN) to all the selected correlation functions and to avoid averaging the media properties over several wavelengths, we consider only data satisfying $0.5L < \lambda = \frac{c}{f} < 1.25L$. Only the most energetic contributions for each frequency are selected to avoid spurious arrivals. The prominent arrivals are plotted together on a frequency versus velocity diagram. For most of the stations, several Rayleigh modes but only one Love mode are observed, as previously observed by (Ma & Clayton 2016). Our approach is to consider all possible modes in the inversion process to fit as many data as possible and to improve the constraints on the depth-dependence of the velocity model.

An example of the blind selection is shown in Fig.2 for station XI-N117. Clear curves emerge from the scatter of measurements above 0.2 Hz, with a larger scattering of the group velocity measurements observed below this frequency. The latter might be caused by the presence of several modes, by horizontal anisotropy, or by local lateral heterogeneity. The phase velocity measurements do not present such characteristics, primarily because the measurement does not suffer from interference between the energy of modes close to osculation points, and because the propagation paths between the stations are mainly straight lines. To avoid fitting isolated points, we further filter these data by averaging them in frequency and velocity, and by selecting at each frequency only the three clouds of points with highest density. The result of hits averaging are shown as open circles in Figs.2 B and D. It is clear that this approach will lead to an averaged structure as is already the case for low frequency, as discussed previously.

2.1 H/V analysis

Following Sánchez-Sesma et al. (2011), we interpret the H/V spectral ratio in terms of the imaginary part of the GF:

$$\frac{H}{V}(\mathbf{x},\omega) = \sqrt{\frac{\langle |v_1(\mathbf{x},\omega)|^2 \rangle + \langle |v_2(\mathbf{x},\omega)|^2 \rangle}{\langle |v_3(\mathbf{x},\omega)|^2 \rangle}} = \sqrt{\frac{\mathrm{Im}(\mathcal{G}_{11}(\mathbf{x},\omega) + \mathcal{G}_{22}(\mathbf{x},\omega))}{\mathrm{Im}(\mathcal{G}_{33}(\mathbf{x},\omega))}}, \quad (1)$$

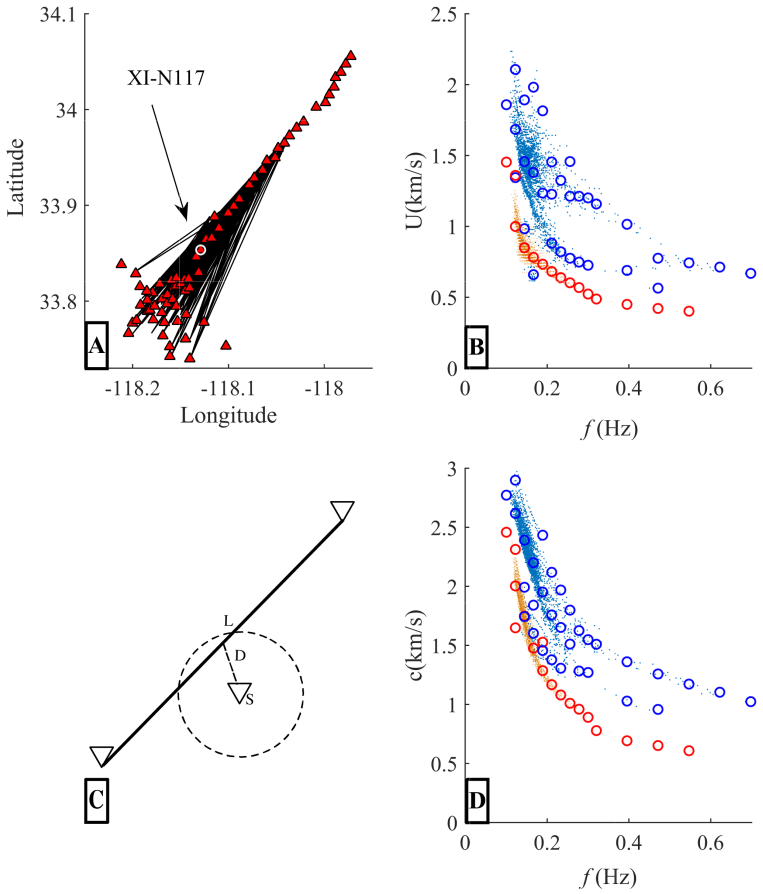

Figure 2. A) All the LASSIE stations (red triangles) and selected station pairs (black rays) around station XI-N117 (white circle) for the DC selection. Group (**B**) and phase (**D**) frequency-velocity diagrams. The original measured velocities from FTAN are depicted as small blue and red points for Rayleigh and Love waves, respectively. The frequency-velocity average of these scattered point-clouds are depicted as empty circles of the same colors. C) Selection of the station pairs located inside an area of 15 km radius centered on station S. For each station pairs ray of length L, the center of the segment must be distant from S by at most a distance $D < L/6$.

where $v_i(\mathbf{x},\omega)$ is the particular velocity spectrum component in the direction i when source and receiver are superimposed at x and for frequency $f = \omega/2\pi$. Components 1 and 2 are in the horizontal plane while component 3 is the vertical. The symbol $\langle\rangle$ denotes the average over multiple time windows. The expression $\left|v_i(\mathbf{x},\omega)\right|^2$ is proportional to the directional energy densities (Perton et al. 2009):

$$E_i = \rho\langle\left|v_i(\mathbf{x},\omega)\right|^2\rangle \tag{2}$$

in direction i and corresponds to the average autocorrelations of the ASF, which under a diffuse field assumption are proportional to the imaginary part of the GF components ($\mathrm{Im}(\mathcal{G}_{ii})$). They are therefore treated as classical ASF cross-correlations, but for the special case when the source and receiver are superimposed. $\mathcal{G}_{ii}(\mathbf{x},\omega)$ is the displacement GF in the direction i at a point $\mathbf{x}$ due to the application of a unit point force in the direction i at the point $\mathbf{x}$. Note that the assumptions underlying eq. 1 differ from other works (e.g., Lin et al. 2012) which usually interpret the H/V ratio as proportional to the Rayleigh wave ellipticity. The latter would be the case only if ASF were composed purely of Rayleigh waves.

Because we are interested in the deep velocity structure of the basin and its geometry, we seek to retrieve low-frequency peaks in H/V. Under the equipartition theorem, the low frequencies are theoretically retrieved more rapidly than the high frequencies (Perton & Sánchez-Sesma 2016). Indeed, a diffuse field can be seen as a superposition of plane waves with propagation directions that cover all available directions. At low frequency, the wavelengths are larger than at high frequency and fewer waves are required to span all the directions effectively. In practice, however, these frequencies may not always be well retrieved since the ASF may be non-diffuse (e.g., Liu & Ben-Zion 2017) and noise sources or secondary sources such as scatterers are not isotropically distributed. Appropriate signal processing, which includes larger time windows and long-time

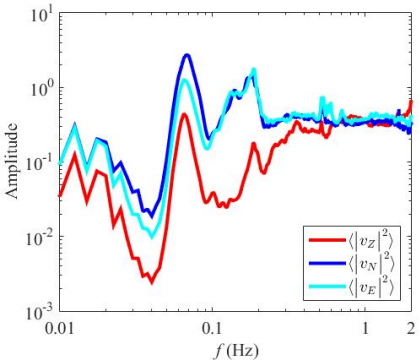

Figure 3. Quantities proportional to the directional energies at station XI-N101. (The density is omitted.)

averaging must be applied to obtain stable and reliable low-frequency peaks in H/V.

For each ASF record, we select time windows of 500 s. Each window is tapered by a 5% cosine function to avoid strong frequency leakage, de-meaned, de-trended, band-pass filtered from 0.05 to 2 Hz, and overlapped by 90%. We apply spectral whitening to each window to enhance equipartitioning of the wavefield (e.g Bensen et al. 2007). Because different sources will act in different frequency bands, the whitening consists of normalizing the signals by the source energies computed from the three components in each time window (i.e. source deconvolution) across different frequency bands (Perton et al. 2017) as:

$$\tilde{v}_i(\mathbf{x},\omega) = v_i(\mathbf{x},\omega) / \sqrt{\frac{\sum_{j=1}^{N_\omega}}{N_\omega} \sum_{i=1}^{3} |v_i(\mathbf{x},\omega_j)|^2}. \tag{3}$$

Here, the ω_j with $j = 1, N_\omega$ belong to $\Delta\omega$, the frequency band centered on ω and of variable width. The width is taken larger than the width of two or three peaks of the directional energies (see Fig. 3) in order to not modify their relative amplitude since they are related to the Green's function, but narrow enough to remove the seismic source signature, i.e. their spectral envelope which is assumed much larger than the oscillations of the Green's function. Because the frequency band is relatively large in this study (i.e., 0.01 to 2 Hz) and because the peaks in the H/V spectra have almost the same width when plotted on a logarithmic frequency axis (Piña-Flores et al. 2016), $\Delta\omega$ is taken to be frequency dependent as $\Delta\omega = \omega/2$.

We compute the autocorrelation of each time window as the square of the absolute value and average over several days. Tests reveal that 5 days of data gives essentially the same results as 40 days. The directional energies for station XI-N101 are presented in Fig. 3. The two horizontal directional energies are similar above 0.1 Hz but differ below that frequency. This could be explained by the presence of heterogeneity or topography that reflects the energy; however, we believe that the main effect is more likely to be the non-isotropic ASF illumination. The shear velocities of the CVM-H model are higher than 1 km/s for depths sampled by frequencies below 0.1 Hz such that the corresponding wavelengths are at least 10 km. The ASF generated from the interaction between the ocean and the coast will be highly unidirectional (e.g., Roux & Ben-Zion 2017). In fact, the largest difference between the two horizontal energy densities is obtained by rotating them by an angle of 5 degrees clockwise, i.e. the South-North components show higher amplitude, which is consistent with the fact that close to Long Beach (point A), the shore is nearly east-west. The ratios between the horizontal components at low frequency (¡0.1 Hz) vary for all the stations of LASSIE 1 (red triangles in Fig.1) and reach up to a factor of 4 for some locations and some frequencies; however, for inland stations, the two horizontal components show similar amplitude, suggesting a more homogeneous ASF source illumination (e.g., Liu & Ben-Zion 2017).

Additionally, as discussed in Perton et al. (2017), the directional energies are equal to the imaginary part of the GF times a factor of frequency raised to a power of D, which depends on the ASF illumination: $E_i \propto -f^D \mathrm{Im}(\mathcal{G}_{ii})$ with $D = 1$ when the field is diffuse in three dimensions (3D) and $D = 2$ in two dimensions (2D). The comparison of the individual components

$$\begin{cases} H = \sqrt{E_1 + E_2} \\ V = \sqrt{E_3} \end{cases} \quad \text{with} \quad \begin{cases} \sqrt{-f^D \mathrm{Im}(\mathcal{G}_{11} + \mathcal{G}_{22})} \\ \sqrt{-f^D \mathrm{Im}(\mathcal{G}_{33})} \end{cases} \tag{4}$$

can be used to identify the factor D in different frequency bands as discussed in section 5.

Finally, the H/V measurements are obtained by applying eq. 1. Three H/Vs are shown in Fig. 4A, as well as their upper and lower bounds calculated from the maximum and minimum values at each frequency of the auto-correlations computed with half of the total number of windows.

The narrow confidence intervals for frequencies above 0.1 Hz (see Fig. 4A) demonstrate the good convergence of the H/V after stacking (e.g. Spica et al. 2017b). The quality of H/V retrieval in this frequency band is further verified by the spatial continuity of the spectral H/V amplitude along the line A–A' (Fig. 4C), where we observe that the H/V shapes change

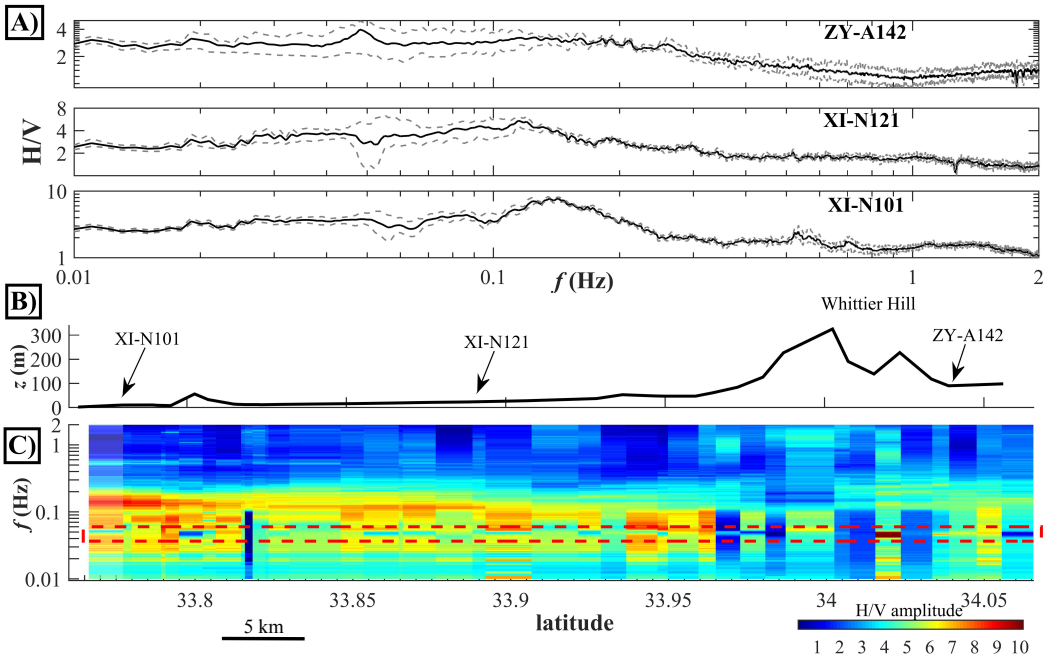

Figure 4. A: Three examples of H/V calculated at stations XI-N101, XI-N121 and ZY-A142 with their respective upper and lower bounds. B: Elevation at seismic stations along the same line. C: Amplitude representation of all the H/V along the line A–A' presented in Fig. 1 and in function of frequency. The red dashed rectangle highlights an anomalous amplitude .

smoothly from station to station. We only observed a discontinuous variation (anomalous high amplitude above 0.1 Hz and low amplitude below 0.1 Hz) near Whittier. As discussed, in section 4, this feature might result from topographic effects generating interference between incident surface-waves and their reflections. Because we assume a local 1D structure during the inversion, topographic effects on H/V (e.g., Molina-Villegas et al. 2018; Maufroy et al. 2018) are beyond the scope of this paper.

The observed confidence intervals are large below 0.1 Hz in (Fig. 4A), even with 40 days of record. The lack of convergence is unrelated to the number of windows used, and is not due to the difference between the two horizontal energy densities. Instead, we explain this by the presence of an anomalous feature between 0.04 and 0.06 Hz, either positive in the H/V of station ZY-A142 either negative in the H/V of stations XI-N121 and XI-N101 shown in Fig. 4A. We also highlighted this anomaly in Fig. 4C with a red dashed rectangle where amplitudes vary discontinuously. This feature comes from very strong oscillations in the energy densities (Fig. 3), highlighting the power of the H/V technique to suppress the effect of ASF anomalies in the energy densities. We will return to this point in section 5. We believe the origin of the oscillations might be related to the strongly non-diffuse nature of the wavefield observed below 0.1 Hz (Liu & Ben-Zion 2017). For these reasons, we decided to avoid this part of the spectrum and carry out the H/V inversion for a bandwidth between 0.1 and 2 Hz.

3 1-D JOINT INVERSION

Individually, the inversion of H/V or of the DC lead to non-unique solutions (e.g. Piña-Flores et al. 2016), but this non-uniqueness can be reduced significantly by inverting these measurements jointly, due to their complementary sensitivity (e.g. Arai & Tokimatsu 2004; Parolai et al. 2005; Zor et al. 2010; Dal Moro 2011; Piña-Flores et al. 2016; Lontsi et al. 2016; Spica et al. 2018a).

H/V is weakly sensitive to the absolute velocity but carries information on relative velocity levels, and is particularly sensitive to V_S contrasts. It is also a local measurement of the structure along an essentially vertical path under the station. On the other hand, the DC are sensitive to the absolute velocity variation with depth, but are only sensitive to velocities averaged across their sensitivity kernels. The joint inversion of several modes of group (U) and phase (c) velocities should increase depth resolution (e.g., Dziewonski & Anderson 1981). Even if group (U) and phase (c) velocities are related, their joint inversion for shear wave structure gives notably better results than either one individually (e.g., Shapiro & Ritzwoller 2002; Spica et al. 2017a). Because the velocities U and c are computed separately, they also allow a consistency check and are therefore used as independent data with different sensitivity. The DC are the expression of a lateral averaging of the structure

below the small sub-arrays used for their computation, and this effect can be managed through the DC selection process. In contrast to the waves probed with the H/V technique, the surface wave propagation expressed in the DC by separated seismic stations have an essentially horizontal wave vector.
In summary, the DC and H/V provide complementary measurements that reduce the non-uniqueness of the velocity variation with depth because they are sensitive to distinct aspects of the structure.

3.1 Forward calculation

The $\mathrm{Im}(\mathcal{G}_{ii})$ components on the right hand side of eq. 1 are associated with an assumed locally horizontal layered structure that varies only with depth. We use the discrete wave number (DWN) method (Bouchon 2003) for the theoretical calculation of the H/V (e.g. Sánchez-Sesma et al. 2011; Spica et al. 2017b; Perton et al. 2017) and the scheme presented by Perton & Sánchez-Sesma (2016) for the DC computation.
As in (Spica et al. 2018a), the bandwidth of the H/V considered in this study spans almost two orders of magnitude with H/V peaks at both low and high frequencies (Fig 4). Proper fitting of the entire spectrum would require a large number of layers to represent the entire velocity profile. The resulting large number of degrees of freedom introduces numerical instabilities in the GF calculation (Perton & Sánchez-Sesma 2016), and considerably slows the inversion. To mitigate these issues we simplify the representation of the velocity structure at each frequency considered during inversion according to the body and surface wave wavelengths and reduce it at the depth for which there is little sensitivity (typically five times the surface wave wavelength) (Perton et al. 2017; Spica et al. 2018a). For this reason, at high frequency, only the shallow part of the structure is considered and at low frequency the smaller, shallow layers are merged while conserving wave propagation times.

3.2 Objective function

Joint inversion of the measurements presents several challenges because we must capture the available information in both the DC and H/V through appropriate weighting (e.g. Spica et al. 2018a): DC and H/V have different units, sampling rate, and scaling. Furthermore, because the Rayleigh and Love modes are of variable quality, the number of modes extracted varies from one site to another. Definition of an appropriate objective function is therefore an important step in converging to stable results. Adding constraints, particularly accurate prior information (if available), can help regularize the problem.
We form the misfit function ε_{HV} relative to the H/V measurements as:

$$\varepsilon_{HV}^2 = \frac{1}{N^{HV}} \sum_{f_{min}^{HV}}^{f_{max}^{HV}} \left(\frac{{}^{H}\!/\!_{V}{}^{obs}(f) - {}^{H}\!/\!_{V}{}^{th}(f)}{{}^{H}\!/\!_{V}{}^{obs}(f)} \right)^2 . \tag{5}$$

The misfit function ε_{DC} relative to the surface wave dispersion includes the group (U) and phase (c) velocity DC for the fundamental (index 0) and higher-modes (index $n > 0$) Rayleigh wave, but only the fundamental Love wave:

$$\varepsilon_{DC}^2 = \frac{1}{N^{DC}} \sum_{f_{min}^{DC}}^{f_{max}^{DC}} \begin{pmatrix} \sum_{n_{Ray}=0}^{2} F^2 \left(U_{Ray}^{obs}(f) - U_{n_{Ray}}^{th}(f) \right) + \\ \sum_{n_{Ray}=0}^{2} F^2 \left(c_{Ray}^{obs}(f) - c_{n_{Ray}}^{th}(f) \right) + \\ F^2 \left(U_{Love}^{obs}(f) - U_{n_{Love}=0}^{th}(f) \right) + \\ F^2 \left(c_{Love}^{obs}(f) - c_{n_{Love}=0}^{th}(f) \right) \end{pmatrix}, \tag{6}$$

with

$$F(x) = \begin{cases} x, & \text{if } x < \text{threshold} \\ \text{threshold} - x, & \text{if threshold} < x < 2\text{threshold} \\ 0, & \text{otherwise.} \end{cases}$$

The threshold is here equal to 250 m/s. Since some points in the FTAN might be associated to reflected surface waves or body wave arrivals, the purpose of the threshold is to avoid that these anomalous points have a contribution to the error. Finally, to estimate the shear velocities and layer thicknesses at each station, we seek to minimize an objective function ε that combines components for H/V and DC:

$$\varepsilon = \sqrt{C^{HV}\varepsilon_{HV}^2 + C^{DC}\varepsilon_{DC}^2}. \tag{7}$$

Observed and theoretical quantities are denoted by the superscripts ^{obs} and th, respectively. The normalization factors C_{HV} and C_{DC} are used to account for the different physical units and control the relative influence of H/V versus DC in the

analysis. Here, a slightly higher weight is given to the H/V to emphasize vertical layering. These weights are equal for all the positions and are fixed so that $C^{HV}\varepsilon_{HV}^2 \approx 2C^{DC}\varepsilon_{DC}^2$ at the lowest misfit when optimizing the structure related to the first inversion. The misfit of dispersion curves is used for regularization to reduce non-uniqueness. N^{HV} and N^{DC} are the number of frequencies, which are sampled logarithmically and linearly respectively between the frequency bounds f_{min} and f_{max}. Because we carry out no explicit mode identification, the input data for dispersion curves are not interpolated and only data points close to the frequency sampled by the theoretical curves are considered (Spica et al. 2018a).

3.3 Parameterization

We used the CVM-H model as a starting point. Because this model is smoothed with more than one hundred layers, we simplified the structure by averaging the propagation times to reduce the number of unknowns. From this initial structure, we considered the shear wave velocity V_S as the only free parameter. We do not focus on estimate the density and compressional wave velocity for two reasons. First, both Love and Rayleigh DC and H/V are more sensitive to V_S than to the other parameters (Spica et al. 2015). Second, ground motion prediction models rely mainly on the shear-wave velocity structure, and the the density and compressional wave velocity can be related to V_S through empirical relationships of polynomial form (Berteussen 1977; Brocher 2005).

We use a constrained nonlinear optimization procedure (Byrd et al. 1999) to minimize Eq. 7 (ε). The constraints consist in limiting the velocity variations between adjacent layers to 25% and to impose the half-space velocity as the highest velocity of the model in order to have a stable computation of the DCs. However, when considering a large number of layers, the sensitivity to the parameters decreases. To reduce this effect, the inversion is performed iteratively following the approach described in Spica et al. (2016) – i.e., a layer is inserted between the two layers showing the highest sensitivity (misfit variation for a given velocity variation) – and we estimate only the parameters of the five surrounding layers (two on each side of the inserted layer). This process is repeated iteratively until an acceptable value of ε , or a maximum number of iterations (10) is reached. Consequently, the thicknesses of the layers are not optimized directly but are modified iteratively and adaptively. After an inversion, the output is used as the input velocity model for the closest new profile to analyze.

4 RESULTS AND DISCUSSION

4.1 Testing the inversion at station XI-N117

Although the joint inversion increases the number of constraints, the identification of a satisfactory model that fits all the measurements is not guaranteed. As an example, we show in Fig. 5 the associated DC and H/V for station XI-N117 calculated from the CVM-H model at the same position. The three first Rayleigh modes fit some of the targets in the frequency band 0.1–1 Hz and the H/V also matches for the whole spectrum (0.02–2 Hz). However there are three issues regarding the DC. First, the theoretical Love DCs (brown lines) are all far from the measurements (red points). Second, the third Rayleigh mode does not fit the measurements below 0.5 Hz for phase velocity and below 0.2 Hz for group velocity. Third, according to the theoretical phase velocity frequency diagram for this velocity structure, the first Rayleigh mode should be strong across the whole frequency band (see Fig. 6); however we do not retrieve measurements for this mode above 0.2 Hz in the frequency-time analysis.

To address these issues, we first conducted an isotropic inversion, following the modes identified in Fig. 2, but we were unable to reduce the misfit. In a second attempt, we introduced anisotropy and conducted an inversion of the Love DC independently from the Rayleigh DC as in Ma & Clayton (2016) and Spica et al. (2017a) without considering the H/V; however, this led to unreliable results with unreasonably strong anisotropy (note that such approaches are only valid for weak anisotropy (Xie et al. 2013)).

Despite the good fits observed on the DC and H/V when using the CVM-H model, we conducted an inversion without prior mode identification and obtained the agreement to the data shown in Fig. 7. The H/V agreement is excellent, particularly for frequencies above 0.3 Hz. Rayleigh and Love mode phase velocities fit better with the targeted points, and the improvement is apparent at low frequencies compared to the DC for the CVM-H model. Surprisingly, the Rayleigh DC fit is obtained using different modes from the ones associated with the CVM-H model: the fundamental (f_0) and first higher modes (f_1) related to our model are strongly superimposed with the first (f_1) and second (f_2) higher modes computed from the CVM-H model. We have two reasons to support our model: 1) The energy of the modes on the theoretical 'phase velocity-frequency' diagram for our resulting velocity structure (Fig. 6 right panel) agrees with the observations, as there is no observed velocity around 0.5 km/s above 0.4 Hz. Furthermore, since the density of observed velocity in Fig. 2D is a measure of the energy, the highest densities coincide with the highest predicted energy; 2) Fundamental Love and Rayleigh wave group DCs are also in good agreement with the estimated velocities, although the fit to higher mode Rayleigh group DCs is not as good. This might be due to the presence of several osculation points where energy leaks between mode branches (Tokimatsu et al. 1992). The phase diagram includes several measurements (blue points) between 0.1 and 0.2 Hz that are not fit by the Rayleigh DC. These

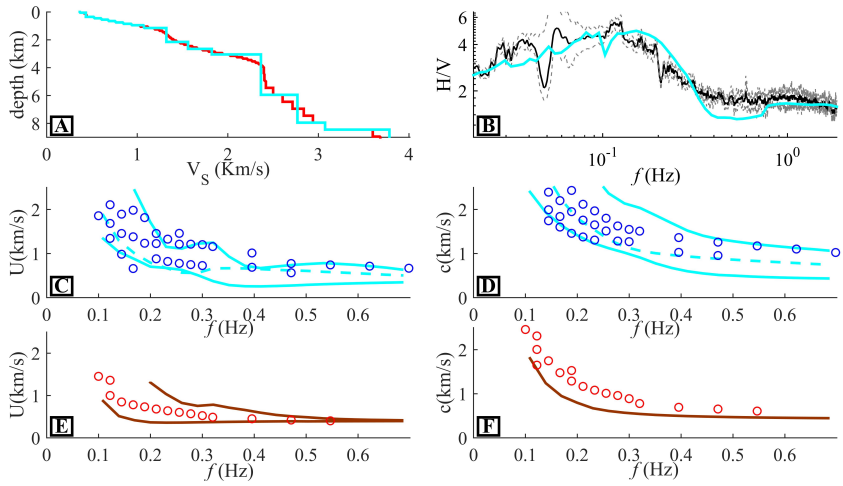

Figure 5. Observed DC and H/V and their theoretical counterparts computed from the CVM-H model at station XI-N117. **A)** CVM-H V_S model (red) under station XI-N117 and harmonically averaged CVM-H V_S model (cyan) used to compute the theoretical H/V and DCs. **B)** Experimental H/V (black line) with its lower and upper bounds (gray lines) and theoretical H/V (cyan). Group (**C**) and phase (**D**) frequency-velocity diagrams for Rayleighs waves (blue circles) and group (**E**) and phase (**F**) frequency-velocity diagrams for Loves waves (red circles). Theoretical DCs are also shown in cyan lines for Rayleigh waves (the second mode is shown as a dashed line to help its identification) and in brown lines for Love modes.

points might be associated with surface wave reflections since they are not present in the data at nearby stations.
The V_S profile is displayed in log-log scale in order to facilitate comparison with the original V_S profile from CVM-H model (Fig. 9). Our V_S profile is higher by about 20% for the uppermost kilometer. At greater depths both models agree well. The size of the layers in our model appear similar with depth, but because of the log scale, this means that the solution has thicker layers with depth. The confidence interval (obtained by the models having a misfit error 50% larger than the best solution) is also larger with increasing depth. This is due to the loss of sensitivity with depth. Nonetheless, this result demonstrates the possibility of obtaining structure to 10 km, which is the deepest structure yet inferred using the H/V technique.

4.2 2D V_S model along the LASSIE array

Now that we have established that our approach retrieves reliable results where the CVM-H model is in relatively good agreement with the observed data, we carried out the inversion for all the positions to a depth of 10 km and over a frequency band of 0.1–2.0 Hz. Several 1D inversion results are shown in Fig. 8 and the full section of the shear velocity along the profile

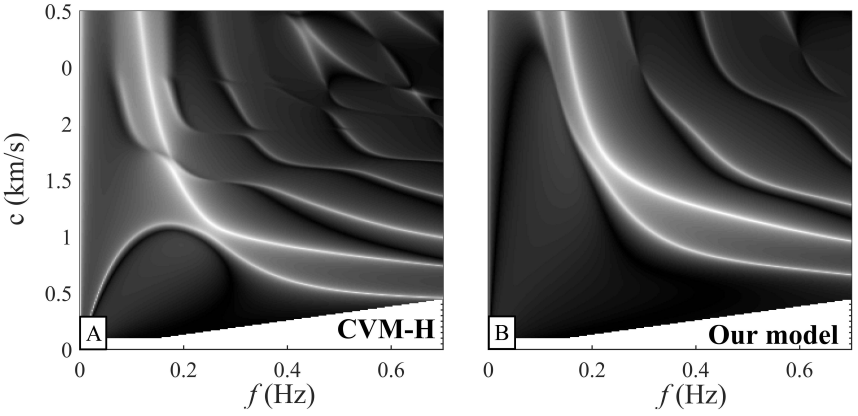

Figure 6. Phase velocity diagrams (c, f) computed from the CVM-H model (A) and our optimized model (B). The two panels were obtained by simulating the wave propagation with the DWN method. Since, the light shades are associated with higher energy comparing to dark shades, the lines correspond to the dispersion curves. In both panels, the highest energy appears approximately at the same location but are due to different modes. In left panel, the highest energy jumps continuously from first to second higher modes and in the right panel this feature is obtained from the contributions of the fundamental and first higher mode.

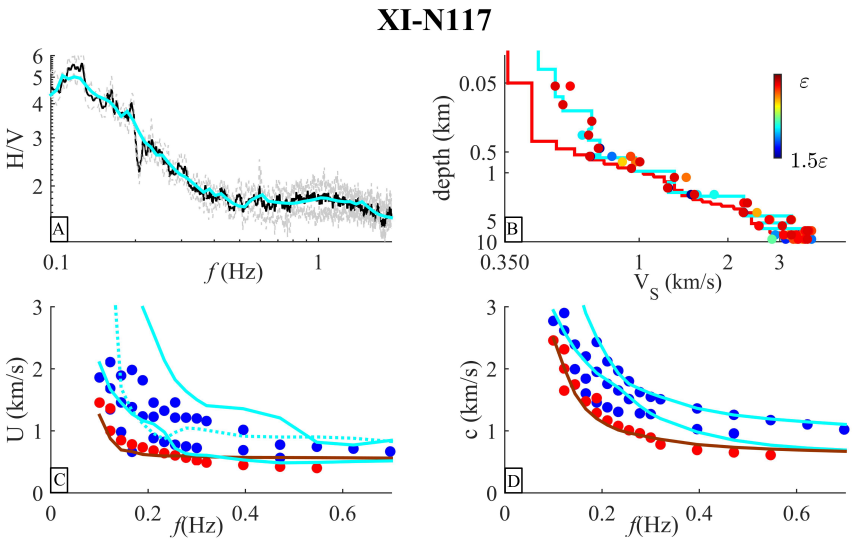

Figure 7. A) Experimental H/V (black line) with its lower and upper bonds (gray lines) and best H/V given by the inversion (cyan). B) original CVM-H (red) and optimized (cyan) models for V_S profile at station XI-N117 in function of depth. The points around the optimized profile represents alternative models with a misfit within 1 to 1.5 times the best misfit. C) Measured (points) and theoretical (lines) Rayleigh (blue points and cyan lines) and Love (red points and brown lines) for group velocities. D) Same as C but for phase velocities.

A–A' is presented in Fig. 9, along with the same section of the CVM-H model. We show the results only to 6 km depth based on the confidence intervals but the 10 km limit was necessary during the inversion to avoid a trade-off with deeper velocity structure. Indeed, the sensitivity to velocity structure from 6 to 10 km deep is sufficient to contaminate shallow structure if we remove the deep structure, but not sufficient to ensure reliable assessment. For all the positions, the fit of the H/V and of the phase velocities are excellent. As for station XI-N117, the fit to group velocities is not straightforward to verify due to the large quantity of data, and because of the DC osculations, but in general, the fit is good for the Rayleigh and Love fundamental modes, and somewhat diminished for higher Rayleigh modes. Nonetheless, for XI-N102 and XI-N111 stations, higher ($n_{Ray} = 3$ and $n_{Ray} = 4$) modes seem also to match the data even though they are not considered during the inversion. The V_S models show a clear continuity along the line A–A'. Our result is not spatially smoothed and therefore may seem less appealing than the CVM-H model, which is smoothed both horizontally and vertically. We preferred showing it without smoothing to convey the details shown on individual V_S profiles shown in Figs 7 and 8. The best agreement with the CVM-H is obtained for station XI-N111. Our results validate the H/V technique with real data and against a model obtained from other techniques. To our knowledge, this is the first time that a validation of the H/V technique under the diffuse field assumption is reported for such deep structure. The largest discrepancy occurs for latitude greater than 34° and in particular for station ZY-A144 where the group and phase velocity plots (Fig. 8) at this location shows more DC points than elsewhere, and these points seem to depict several Love modes. The 34° discrepancy is well observed on the right part of the Fig. 9. We suspect that some of these points are the consequence of surface wave scattering due to lateral heterogeneities such as Whittier Hill. In that case, the reflected waves are delayed with respect to the direct arrivals, and our DCs converge toward the points with the highest apparent velocities only. This suggests that the use of joint DC and H/V inversion may allow the identification of reflected surface waves.

In order to compare our model to documented geological features of the region, we superimposed the main geological features of a geological profile that is close to the A-A' profile (E-E' in Wright 1991) to our model section. Certain heterogeneities and layer thickness shortening agree well with the presence of faults near Long beach or near Whittier fault. While observing fault structure from surface wave tomography is challenging (e.g., Mordret et al. 2018), the high density of the LASSIE array and our processing allows to highlight such features with relative confidence. The LA basin shape, with low velocity in the center (red to yellow) agrees well with the geometry proposed by (Wright 1991). Note that the V_S velocity in CVM-H was largely inferred from the P-wave velocity from the industry, such that much of the detail reflects V_P and is less constrained for absolute V_S. In contrast, our model provides new measurements of the shear velocity.

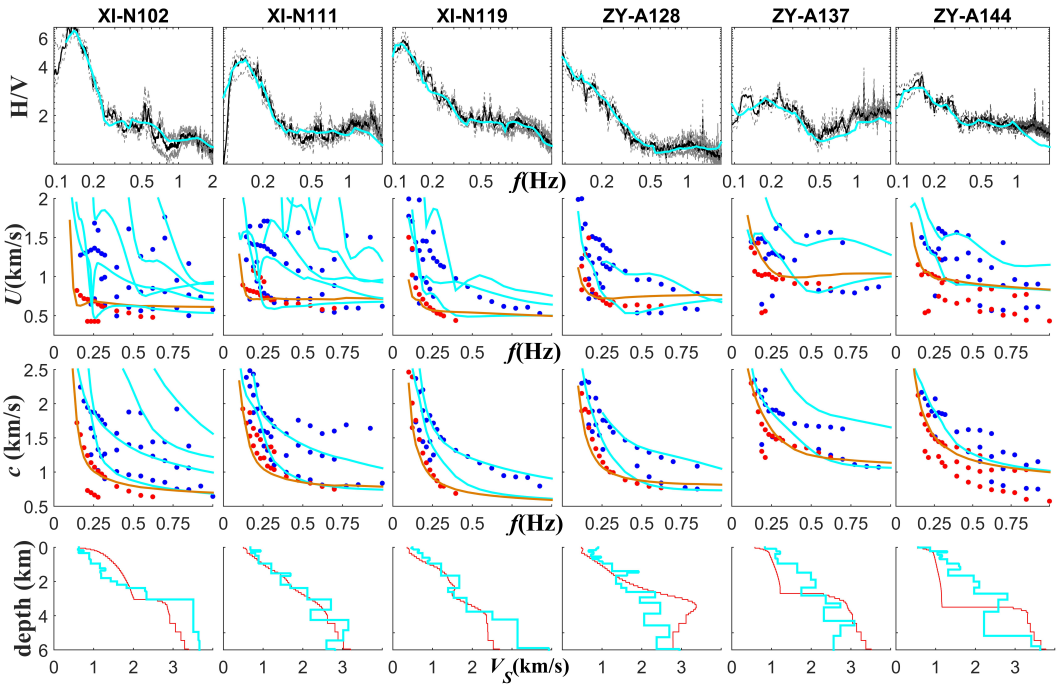

Figure 8. Examples of 1D joint inversions at different sites. The station ID is shown on top of each column. Top row of panels shows the observed H/V (black lines) with its lower and upper bounds (gray lines) and the theoretical counterpart (cyan lines). In the second and third row of panels, we show respectively the group and phase velocity fits with the results of FTAN average for Rayleigh velocities (blue points) and Love velocities (red points) with the theoretical DCs (cyan for Rayleigh and brown for Love). In the lower panels , we show the CVM-H model (red lines) and our estimated shear velocity model (cyan lines).

5 PERSPECTIVE: ASSESSING MOHO DEPTH

Although we limited the depth of the inversion to 10 km, the H/V technique has the power to detect deeper structure. Indeed, for certain stations (e.g., XI-N110. Fig. 10), the H/V confidence interval in the low frequency band (0.02–0.1) Hz is less than 30 % of its amplitude (except for the problematic 0.04–0.06 Hz frequency band previously mentioned), which suggests they can be used to conduct a reliable inversion, however, there are several complicating factors.

First, we do not have DC information in this frequency band, giving weaker constraints on the absolute velocities (section

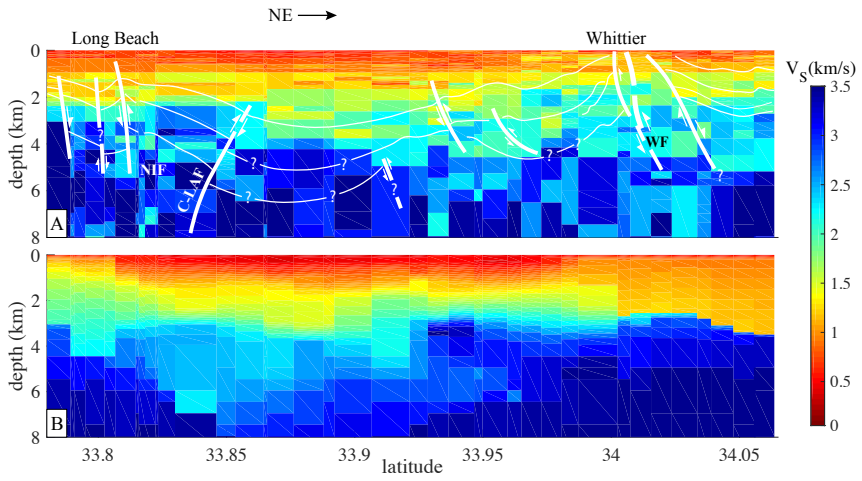

Figure 9. V_S sections along the line A–A' from our model (A) and from CVM-H model (B). The geological features superimposed at scale on our model are taken from (Wright 1991, Fig. S1 in the Supporting Information). WF: Whittier Fault; C-LAF: Compton-Los Alamitos Fault; NIF: Newport-Inglewood Fault.

3); however, the shallow part of the model (i.e. the 10 first km) is already well constrained by our previous inversion, so the results of the new inversion are expected to be only weakly biased (e.g., Spica et al. 2018a).
Second, because the H/V technique is more sensitive to velocity contrasts, the constant velocity indicated by the CVM-H model between 15-22 km depth (Fig. 10B) is difficult to retrieve and our iterative inversion process converges to a V_S profile with several layers describing an unrealistically large oscillation and large confidence interval. We modified the iterative process and further merge the layers showing large confidence intervals while refining layers that are better considered by data.
Finally, the two horizontal components of the energy densities have different amplitudes due to the ASF illumination being predominantly unidirectional at low frequencies. As discussed in (Perton et al. 2017), a solution consists in adapting the forward modeling of the H/V by considering wave propagation in a two dimensional plane defined by the ASF illumination direction (i.e. the South-North direction noted here $\mathbf{e_{SN}}$) and the vertical direction. We projected the horizontal components of the energy densities in ($\mathbf{e_{SN}}$) direction and the result is noted H_{SN}. To allow the continuity of the H/V across the different frequency bands, we compute H/V as $2H_{\mathrm{SN}}/V$.
The resulting observed H/V at XI-N110 station is presented in Fig. 10 along with its theoretical counterpart computed from the optimized model. To confirm that the ASF illumination is effectively 2D, we present the individual contributions $E_{H_{\mathrm{SN}}}$ and E_V and compare them with the modified imaginary part of the GF (i.e. $-f^D\mathrm{Im}(\mathcal{G}_{ii}$ in eq. 4). Due to the presence of an unknown coefficient of proportionality in Eq. 4, these curves are all normalized to one in the high frequency part ([0.2–2 Hz]) (Perton et al. 2017) by dividing by their respective maxima (e.g. ${}^{E_V(f)}/_{max(E_V(f\,\in\,[0.2,\,2Hz]))}$). The choice of the range of frequency is to avoid making a normalization subject to abnormal amplitude variation at low frequency. The high frequency part ($f > 0.1$ Hz) is obtained with $D = 1$ and fits well the observed data. For the low frequency part ($f \leq 0.1$ Hz), we present the results obtained with $D = 2$ (continuous line) and with $D = 1$ (dashed line). Besides the presence of the large oscillations, it is clear the simulation with $D = 2$ (i.e. assuming 2D wave propagation) can represent the trend of the data. The comparison of the individual E_H and E_V components allows us to characterize the degree of diffusivity of the ASF illumination. On the other hand, the theoretical H/V computed with $D = 2$ and with $D = 1$ in a horizontally unbounded medium are nearly identical, supporting the idea that computing H/V from ASF does not require a perfectly isotropic illumination. This is a notable advantage comparing to ASF cross-correlation techniques using two separated receivers, in which non-isotropic illumination can be strongly detrimental to the results (Bensen et al. 2007; Tsai 2009).
The resulting V_S profile is very similar to the CVM-H model between 7–30 km. Also, the Moho depth is well retrieved by our inversion (at approximately 22 km). We allow several layers around the discontinuity in order to allow the depth assessment since the thicknesses are not optimized. Although this model suffers from weak sensitivity to absolute velocity, it confirms that we can retrieve the depth of the strong and deep impedance contrast across the Moho through H/V observations. In fact, the observed H/V and the computed H/V using CVM-H models show a peak at similar low frequency for most of the stations although we obtained coherent amplitude for only 8 stations. This suggests that after reliable and careful computation of the low frequency H/V, the method could be used as a tool to constrain the depth of deep interfaces, in a similar way receiver functions are used. The main advantage of H/V over receiver functions is that it can be performed with short deployments of temporary a array (only a few days of data are required) to obtain the necessary information, and it does not rely on recording a distribution of large teleseismic earthquakes for signals.

6 CONCLUSION

We used data from a dense, short duration broadband array deployed across the LA Basin to image the V_S structure of the basin based on a diffuse field approach. We computed multimode DCs for both Rayleigh and Love waves and also H/V spectral ratios. We extracted phase and group DCs from cross-correlation of ASF and H/Vs from its autocorrelation. These five sets of measurements were used to estimate the 1D velocity structure at each of the 40 sites of the linear array. The joint use of these measurements helps reduce the trade-off between velocity and layer thickness, and gives enhanced depth sensitivity to the model. The resulting velocity model provides new and independent constraints on V_S for an area for which S-wave velocity was previously largely inferred indirectly from P-wave velocity.
For the most part, our model agrees extremely well with CVM-H model, confirming both the utility of the diffuse field H/V measurements for deep structural characterization and the predictive value of the CVM-H community velocity model in the Los Angeles region. Our analysis yields a consistent structural picture of the subsurface in agreement with other data, and it also highlights strong vertical and lateral heterogeneity in the shallow subsurface. Finally, analysis of low frequency peak in the H/V ratio showed promising results toward Moho depth characterization, which could be achieved through much shorter deployments than required for receiver function analysis.

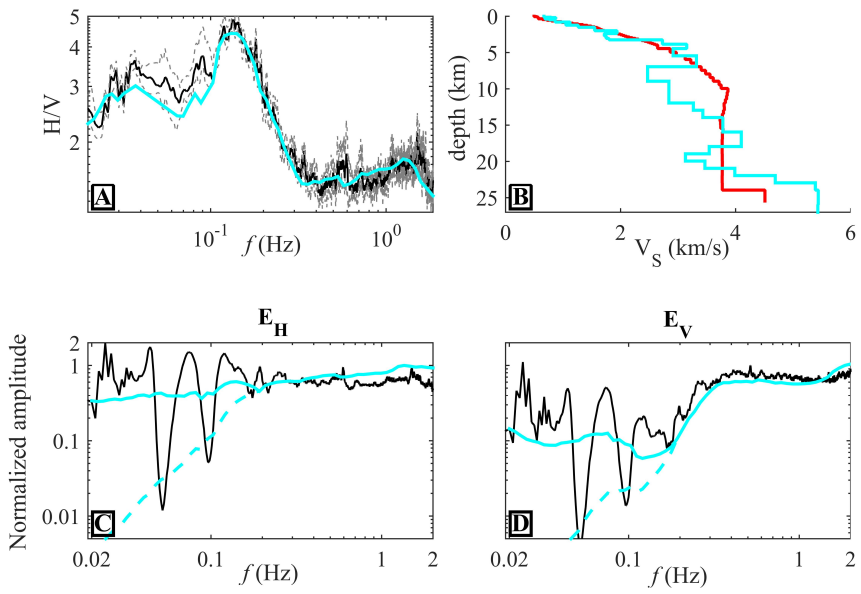

Figure 10. Example of 1D inversion at station XI-N110 that includes low frequencies. **A)** Observed H/V (black line) with its lower and upper bounds (gray lines) and theoretical H/V associated to the best inverted model (cyan). **B)** original CVM-H (red) and optimized (cyan) V_S models as functions of depth. Bottom: Observed energy densities (black lines) for horizontal component **C)** and vertical component **D)** along with their respective theoretical counterpart (cyan). These latter correspond to the imaginary parts of the GF times frequency raised to a power of one above 0.2 Hz. Below that frequency, the power is equal to 1 (dashed line) or 2 (continuous line). All the energy densities are normalized to one in the frequency band 0.2–2 Hz.

7 ACKNOWLEDGMENTS

We thank Jorge Castillo Castellanos for providing us the Green's functions computed by Yiran Ma. This research was supported by the Southern California Earthquake Center (Contribution No. 9096). SCEC is funded by NSF Cooperative Agreement EAR-1600087 & USGS Cooperative Agreement G17AC00047. We thank the partners of the LASSIE survey: Nodalseismic (Dan Hollis and Mitchell Barklage), USGS (Elizabeth Cochran), UCLA (Paul Davis) and CalPoly Pomona (J. Polet). The authors are grateful for the editorial work of Andrea Morelli and thorough reviews from Michael Asten and another anonymous referee.

REFERENCES

Arai, H. & Tokimatsu, K., 2004. S-wave velocity profiling by inversion of microtremor H/V spectrum, *Bulletin of the Seismological Society of America*, **94**(1), 53–63.

Asten, M. W., Askan, A., Ekincioglu, E. E., Sisman, F. N., & Ugurhan, B., 2014. Site characterisation in north-western Turkey based on SPAC and HVSR analysis of microtremor noise, *Exploration Geophysics*, **45**(2), 74–85.

Bensen, G. D., Ritzwoller, M. H., Barmin, M. P., Levshin, A. L., Lin, F., Moschetti, M. P., Shapiro, N. M., & Yang, Y., 2007. Processing seismic ambient noise data to obtain reliable broad-band surface wave dispersion measurements, *Geophysical Journal International*, **169**(3), 1239–1260.

Berg, E., Lin, F.-C., Allam, A., Qiu, H., Shen, W., & Ben-Zion, Y., 2018. Tomography of Southern California via Bayesian joint inversion of Rayleigh wave ellipticity and phase velocity from ambient noise cross-correlations, *Journal of Geophysical Research: Solid Earth*, **123**(11), 9933–9949.

Berteussen, K. A., 1977. Moho depth determinations based on spectral-ratio analysis of NORSAR long-period P waves, *Physics of the Earth and Planetary Interiors*, **15**(1), 13–27.

Bouchon, M., 2003. A review of the discrete wavenumber method, *Pure and applied Geophysics*, **160**(3-4), 445–465.

Bowden, D., Tsai, V., & Lin, F., 2015. Site amplification, attenuation, and scattering from noise correlation amplitudes across a dense array in long beach, ca, *Geophysical Research Letters*, **42**(5), 1360–1367.

Brocher, T. M., 2005. Empirical relations between elastic wavespeeds and density in the Earth's crust, *Bulletin of the Seismological Society of America*, **95**(6), 2081–2092.

Byrd, R. H., Hribar, M. E., & Nocedal, J., 1999. An interior point algorithm for large-scale non-linear programming, *SIAM Journal on Optimization*, **9**(4), 877–900.

Cruz-Atienza, V., Tago, J., Sanabria-Gómez, J., Chaljub, E., Etienne, V., Virieux, J., & Quintanar, L., 2016. Long duration of ground motion in the paradigmatic valley of mexico, *Scientific reports*, **6**, 38807.

Dal Moro, G., 2011. Some aspects about surface wave and HVSR analyses: a short overview and a case study., *Bollettino di Geofisica Teorica ed Applicata*, **52**(2).

Denolle, M., Dunham, E., Prieto, G., & Beroza, G., 2014. Strong ground motion prediction using virtual earthquakes, *Science*, **343**(6169), 399–403.

Denolle, M. A., Dunham, E. M., & Beroza, G. C., 2012. Solving the surface-wave eigenproblem with Chebyshev spectral collocation, *Bulletin of the Seismological Society of America*, **102**(3), 1214–1223.

Dziewonski, A. M. & Anderson, D. L., 1981. Preliminary reference earth model, *Physics of the Earth and Planetary Interiors*, **25**(4), 297–356.

García-Jerez, A., Piña-Flores, J., Sánchez-Sesma, F. J., Luzón, F., & Perton, M., 2016. A computer code for forward calculation and inversion of the H/V spectral ratio under the diffuse field assumption, *Computers & Geosciences*, **97**, 67 – 78.

Graves, R., Jordan, T. H., Callaghan, S., Deelman, E., Field, E., Juve, G., Kesselman, C., Maechling, P., Mehta, G., Milner, K., et al., 2011. Cybershake: A physics-based seismic hazard model for southern california, *Pure and Applied Geophysics*, **168**(3-4), 367–381.

Hauksson, E., 2000. Crustal structure and seismicity distribution adjacent to the pacific and north america plate boundary in southern california, *Journal of Geophysical Research: Solid Earth*, **105**(B6), 13875–13903.

Jennings, C. & Bryant, W., 2010. Fault activity map of california: California geological survey geologic data map no. 6.

Komatitsch, D., Liu, Q., Tromp, J., Suss, P., Stidham, C., & Shaw, J. H., 2004. Simulations of ground motion in the Los Angeles basin based upon the spectral-element method, *Bulletin of the Seismological Society of America*, **94**(1), 187–206.

LASSIE, 2014. Los Angeles Seismic Syncline Interferometry Experiment, Caltech, Dataset.

Lee, E.-J., Chen, P., Jordan, T. H., Maechling, P. B., Denolle, M. A. M., & Beroza, G. C., 2014. Full-3-D tomography for crustal structure in Southern California based on the scattering-integral and the adjoint-wavefield methods, *Journal of Geophysical Research: Solid Earth*, **119**(8), 6421–6451.

Lin, F.-C., Schmandt, B., & Tsai, V. C., 2012. Joint inversion of rayleigh wave phase velocity and ellipticity using usarray: Constraining velocity and density structure in the upper crust, *Geophysical Research Letters*, **39**(12).

Lin, F.-C., Li, D., Clayton, R. W., & Hollis, D., 2013. High-resolution 3D shallow crustal structure in Long Beach, California: Application of ambient noise tomography on a dense seismic array, *Geophysics*, **78**(4), Q45–Q56.

Liu, X. & Ben-Zion, Y., 2017. Analysis of non-diffuse characteristics of the seismic noise field in southern California based on correlations of neighbouring frequencies, *Geophysical Journal International*, **212**(2), 798–806.

Lontsi, A. M., Sánchez-Sesma, F. J., Molina-Villegas, J. C., Ohrnberger, M., & Krüger, F., 2015. Full microtremor H/V (z, f) inversion for shallow subsurface characterization, *Geophysical Journal International*, **202**(1), 298–312.

Lontsi, A. M., Ohrnberger, M., Krüger, F., & Sánchez-Sesma, F. J., 2016. Combining surface-wave phase-velocity dispersion curves and full microtremor horizontal-to-vertical spectral ratio for subsurface sedimentary site characterization, *Interpretation*, **4**(4), SQ41–SQ49.

Ma, Y. & Clayton, R. W., 2016. Structure of the los angeles basin from ambient noise and receiver functions, *Geophysical Journal International*, **206**(3), 1645–1651.

Ma, Y., Clayton, R. W., & Li, D., 2016. Higher-mode ambient-noise rayleigh waves in sedimentary basins, *Geophysical Journal International*, **206**(3), 1634–1644.

Magistrale, H., McLaughlin, K., & Day, S., 1996. A geology-based 3D velocity model of the Los Angeles basin sediments, *Bulletin of the Seismological Society of America*, **86**(4), 1161–1166.

Magistrale, H., Day, S., Clayton, R. W., & Graves, R., 2000. The SCEC southern California reference three-dimensional seismic velocity model version 2, *Bulletin of the Seismological Society of America*, **90**(6B), S65–S76.

Maufroy, E., Lacroix, P., Chaljub, E., Sira, C., Grelle, G., Bonito, L., Causse, M., Cruz-Atienza, V. M., Hollender, F., Cotton, F., et al., 2018. Towards rapid prediction of topographic amplification at small scales: contribution of the FSC proxy and Pleiades terrain models for the 2016 Amatrice earthquake (Italy, Mw 6.0), in *16th European Conference on Earthquake Engineering, Thessaloniki, Greece, June*, pp. 18–21.

Molina-Villegas, J. C., Jaramillo Fernández, J. D., Piña-Flores, J., & Sánchez-Sesma, F. J., 2018. Local generation of Love surface waves at the edge of a 2D alluvial valley, *Bulletin of the Seismological Society of America*, **108**(4), 2090.

Mordret, A., Roux, P., Boué, P., & Ben-Zion, Y., 2018. Shallow three-dimensional structure of the San Jacinto fault zone revealed from ambient noise imaging with a dense seismic array, *Geophysical Journal International*, **216**(2), 896–905.

Nakamura, Y., 1989. A method for dynamic characteristics estimation of subsurface using microtremor on the ground surface (in japanese with english abstract), *Railway Technical Research Institute, Quarterly Reports*, **30**(1).

Nakata, N., Chang, J. P., Lawrence, J. F., & Boué, P., 2015. Body wave extraction and tomography at Long Beach, California, with ambient-noise interferometry, *Journal of Geophysical Research: Solid Earth*, **120**(2), 1159–1173.

Olsen, K., 2000. Site amplification in the los angeles basin from three-dimensional modeling of ground motion, *Bulletin of the Seismological Society of America*, **90**(6B), S77–S94.

Olsen, K., Day, S., Minster, J., Cui, Y., Chourasia, A., Faerman, M., Moore, R., Maechling, P., & Jordan, T., 2006. Strong shaking in Los Angeles expected from southern San Andreas earthquake, *Geophysical Research Letters*, **33**(7).

Olsen, K., Day, S., Dalguer, L., Mayhew, J., Cui, Y., Zhu, J., Cruz-Atienza, V., Roten, D., Maechling, P., Jordan, T., et al., 2009. ShakeOut-D: Ground motion estimates using an ensemble of large earthquakes on the southern San Andreas fault with spontaneous rupture propagation, *Geophysical Research Letters*, **36**(4).

Parolai, S., Picozzi, M., Richwalski, S., & Milkereit, C., 2005. Joint inversion of phase velocity dispersion and H/V ratio curves from seismic noise recordings using a genetic algorithm, considering higher modes, *Geophysical research letters*, **32**(1).

Perton, M. & Sánchez-Sesma, F. J., 2016. Green's function calculation from equipartition theorem, *The Journal of the Acoustical Society of America*, **140**(2), 1309–1318.

Perton, M., Sánchez-Sesma, F. J., Rodríguez-Castellanos, A., Campillo, M., & Weaver, R. L., 2009. Two perspectives on equipartition in diffuse elastic fields in three dimensions, *The Journal of the Acoustical Society of America*, **126**(3), 1125–1130.

Perton, M., Spica, Z., & Caudron, C., 2017. Inversion of the horizontal-to-vertical spectral ratio in presence of strong lateral heterogeneity, *Geophysical journal international*, **212**(2), 930–941.

Piña-Flores, J., Perton, M., García-Jerez, A., Carmona, E., Luzón, F., Molina-Villegas, J. C., & Sánchez-Sesma, F. J., 2016. The inversion of spectral ratio H/V in a layered system using the diffuse field assumption (DFA), *Geophysical Journal International*, p. ggw416.

Rivet, D., Campillo, M., Sanchez-Sesma, F., Shapiro, N. M., & Singh, S. K., 2015. Identification of surface wave higher modes using a methodology based on seismic noise and coda waves, *Geophysical Journal International*, **203**(2), 856–868.

Roux, P. & Ben-Zion, Y., 2017. Rayleigh phase velocities in Southern California from beamforming short-duration ambient noise, *Geophysical Journal International*, **211**(1), 450–454.

Sánchez-Sesma, F. J., Rodríguez, M., Iturrarán-Viveros, U., Luzón, F., Campillo, M., Margerin, L., García-Jerez, A., Suarez, M., Santoyo, M. A., & Rodríguez-Castellanos, A., 2011. A theory for microtremor H/V spectral ratio: application for a layered medium, *Geophysical Journal International*, **186**(1), 221–225.

Savage, M. K., Lin, F.-C., & Townend, J., 2013. Ambient noise cross-correlation observations of fundamental and higher-mode rayleigh wave propagation governed by basement resonance, *Geophysical Research Letters*, **40**(14), 3556–3561.

Scherbaum, F., Hinzen, K.-G., & Ohrnberger, M., 2003. Determination of shallow shear wave velocity profiles in the Cologne, Germany area using ambient vibrations, *Geophysical Journal International*, **152**(3), 597–612.

Shapiro, N. & Ritzwoller, M., 2002. Monte-Carlo inversion for a global shear-velocity model of the crust and upper mantle, *Geophysical Journal International*, **151**(1), 88–105.

Shapiro, N. M., Campillo, M., Stehly, L., & Ritzwoller, M. H., 2005. High-resolution surface-wave tomography from ambient seismic noise, *Science*, **307**(5715), 1615–1618.

Shaw, J. H., Plesch, A., Tape, C., Suess, M. P., Jordan, T. H., Ely, G., Hauksson, E., Tromp, J., Tanimoto, T., Graves, R., et al., 2015. Unified structural representation of the southern California crust and upper mantle, *Earth and Planetary Science Letters*, **415**, 1–15.

Spica, Z., Caudron, C., Perton, M., Lecocq, T., Camelbeeck, T., Legrand, D., Piña-Flores, J., Iglesias, A., & Syahbana, D. K., 2015. Velocity models and site effects at Kawah Ijen volcano and Ijen caldera (Indonesia) determined from ambient noise cross-correlations and directional energy density spectral ratios, *Journal of Volcanology and Geothermal Research*, **302**, 173–189.

Spica, Z., Perton, M., Calò, M., Legrand, D., Córdoba-Montiel, F., & Iglesias, A., 2016. 3-D shear wave velocity model of Mexico and south US: bridging seismic networks with ambient noise cross-correlations (C^1) and correlation of coda of correlations (C^3), *Geophysical Journal International*, **206**(3), 1795–1813.

Spica, Z., Perton, M., & Legrand, D., 2017a. Anatomy of the Colima volcano magmatic system, Mexico, *Earth and Planetary Science Letters*, **459**, 1–13.

Spica, Z., Perton, M., Nakata, N., Liu, X., & Beroza, G. C., 2018a. Shallow V_s imaging of the Groningen area from joint inversion of multimode surface waves and H/V spectral ratios, *Seismological Research Letters*, **89**(5), 1720–1729.

Spica, Z. J., Perton, M., Nakata, N., Liu, X., & Beroza, G. C., 2017b. Site characterization at Groningen gas field area through joint surface-borehole H/V analysis, *Geophysical Journal International*, **212**(1), 412–421.

Spica, Z. J., Nakata, N., Liu, X., Zijian, T., Campman, X., & Beroza, G. C., 2018b. The ambient seismic field at Groningen gas field: An overview from the surface to reservoir depth, *Seismological Research Letters*.

Süss, M. P. & Shaw, J. H., 2003. P wave seismic velocity structure derived from sonic logs and industry reflection data in the los angeles basin, california, *Journal of Geophysical Research: Solid Earth*, **108**(B3).

Tanimoto, T. & Rivera, L., 2005. Prograde Rayleigh wave particle motion, *Geophysical Journal International*, **162**(2), 399–405.

Tape, C., Liu, Q., Maggi, A., & Tromp, J., 2009. Adjoint tomography of the southern california crust, *Science*, **325**(5943), 988–992.

Tokimatsu, K., Tamura, S., & Kojima, H., 1992. Effects of multiple modes on Rayleigh wave dispersion characteristics, *Journal of Geotechnical Engineering*, **118**(10), 1529–1543.

Tomar, G., Stutzmann, E., Mordret, A., Montagner, J.-P., Singh, S. C., & Shapiro, N. M., 2018. Joint inversion of the first overtone and fundamental mode for deep imaging at the Valhall oil field using ambient noise, *Geophysical Journal International*, **214**(1), 122–132.

Tsai, V. C., 2009. On establishing the accuracy of noise tomography travel-time measurements in a realistic medium, *Geophysical Journal International*, **178**(3), 1555–1564.

Wald, D. J. & Graves, R. W., 1998. The seismic response of the Los Angeles basin, California, *Bulletin of the Seismological Society of America*, **88**(2), 337–356.

Wright, T. L., 1991. Structural geology and tectonic evolution of the los angeles basin, california, *Act. Margin Basins*, **52**, 35–134.

Xie, J., Ritzwoller, M. H., Shen, W., Yang, Y., Zheng, Y., & Zhou, L., 2013. Crustal radial anisotropy across eastern Tibet and the western Yangtze craton, *Journal of Geophysical Research: Solid Earth*, **118**(8), 4226–4252.

Zhu, L. & Kanamori, H., 2000. Moho depth variation in southern california from teleseismic receiver functions, *Journal of Geophysical Research: Solid Earth*, **105**(B2), 2969–2980.

Zor, E., Özalaybey, S., Karaaslan, A., Tapırdamaz, M. C., Özalaybey, S. Ç., Tarancıoğlu, A., & Erkan, B., 2010. Shear wave velocity structure of the Izmit Bay area (Turkey) estimated from active–passive array surface wave and single-station microtremor methods, *Geophysical Journal International*, **182**(3), 1603–1618.